nature communications

Article

https://doi.org/10.1038/s41467-025-59722-1

Unlocking single-atom induced electronic metal-support interactions in electrocatalytic one-electron water oxidation for wastewater purification

Received: 16 December 2024

Accepted: 1 May 2025

A list of authors and their affiliations appears at the end of the paper

Electro-oxidation is a promising green technology for decentralized wastewater purification. However, its efficacy is primarily constrained by the selectivity and efficiency of hydroxyl radical (•OH) generation through one-electron water oxidation. In this study, we elucidate the mechanism of electronic metal-support interactions (EMSI) of Ni single-atoms on antimony-doped tin oxide anode (Ni/ATO) to enhance •OH production and overall water treatment efficiency. We experimentally and theoretically investigate both the structural evolution process and micro-interface mechanisms associated with the EMSI effects induced by Ni single-atoms. The optimized electronic structures in the interfacial catalysts under EMSI conditions and the co-catalytic role of Ni single-atoms synergistically facilitate selective and efficient •OH generation, resulting in over a fivefold increase in its steady-state concentration and tenfold enhancement in pseudo-first-order rate constant of sulfamethoxazole degradation compared to those on bare ATO. With the EMSI, rapid electron transfer channels were established for a marked enhancement in the adsorption, conversion, and dissociation of interfacial H_2O molecules. Notably, it is revealed that Ni single-atoms serve as co-catalytic sites, exhibiting a "H-pulling effect" that is crucial for •OH generation. The Ni/ATO anode demonstrates great efficiency in degrading various refractory organic pollutants, and effectively treats real pharmaceutical wastewater with low energy consumption. Furthermore, it presents remarkable stability and adaptability, while maintaining a minimal environmental footprint during wastewater treatment processes. This work addresses the theoretical gaps between EMSI effects and co-catalysis in electro-oxidation systems, while providing a robust technological solution for wastewater purification.

With the advancement of global industrialization and intensification of human activities, water scarcity and pollution have emerged as critical environmental issues worldwide[1,2]. A variety of refractory pollutants are discharged into the aqueous environment, especially emerging pollutants such as antibiotics and pesticides, are challenging to be degraded effectively through traditional physicochemical and biological treatment technologies due to their chemical stability and low concentrations in wastewater, posing a serious threat to ecosystems

e-mail: zhangguan@hit.edu.cn

and human health[3,4]. Electro-oxidation processes (EOPs) are regarded as a green and efficient advanced-oxidation technology, particularly suitable for decentralized water treatment, as they generate hydroxyl radicals (•OH) with strong oxidizing ability (standard oxidation potential: 2.80 V, half-life: <5 μs) through one-electron water oxidation to achieve harmless treatment of refractory organic pollutants[5,6]. However, EOPs performance is primarily constrained by the catalytic activity of the anode materials in the efficiency and selectivity of •OH generation[7–9]. It is essential to inhibit the thermodynamically favorable four-electron water oxidation reaction that results in the release of O_2[10]. Studies have indicated that "non-active" anodes as ideal electrodes, typically comprising metals or metal oxides like PbO_2/Ti, Sb_2O_5-SnO_2/Ti, Ti_4O_7, exhibit higher O_2 evolution overpotentials while favoring •OH generation along with complete oxidation of organics for wastewater treatment[9,11,12]. Their high catalytic activity arises from weaker interactions between the anode surface and •OH. Based on a proposed model, initial reactions on different anodes correspond to the oxidation of water molecules into physisorbed •OH, avoiding the formation of higher-valence states of metal oxides on the electrode[13]. From this perspective, optimizing the structure and composition of "non-active" anodes to enhance one-electron water oxidation alongside physisorbed •OH generation is crucial for advancing EOPs.

Recently, strong metal-support interactions (SMSI) between metals/oxides and their solid supports have been shown to significantly enhance electrocatalytic activity and stability by enhancing electronic interactions at the metal-support interface[14,15]. For example, a Cu/$CoSe_2$/C electrode demonstrates enhanced electrocatalytic three-electron oxygen reduction reaction (ORR), leading to increased production of •OH due to the SMSI effect[16]. However, conventional SMSI typically relies on nanoparticle's size and encapsulation-structure, which face challenges including limited numbers of active sites coupled with relatively low electron transfer efficiency[17,18]. Encouragingly, single-atom catalysts (SACs), noted for their exceptional atomic utilization rates alongside unique electronic structures, have garnered attention as promising candidates across various fields[19,20]. Consequently, SACs allow for expanding SMSI into electronic metal-support interactions (EMSI), overcoming inherent metal effects at an electronic level. This transition will enhance electrocatalytic performance through improving charge transfer dynamics while regulating adsorption behaviors of intermediates[21,22]. Additionally, the co-catalysis in EMSI, where both the single-atoms and the support-atoms actively participate in the catalytic reaction, presents another intriguing aspect that influences the catalytic mechanism.

Although the EMSI effect has been observed in oxygen/hydrogen evolution reaction (OER/HER) and ORR[23–25], there appears a notable gap in this effect to enhance the water oxidation process to •OH formation in EOPs. Water oxidation can result in either O_2 evolution or •OH formation, with distinct mechanisms and implications. In this context, the development of EMSI, along with unveiling its micro-interfacial mechanisms in boosting •OH generation is crucial but not clearly understood or defined. Furthermore, the contributions and pivotal roles of single-atoms in modulating electronic structures, electron transfer efficiency, and adsorptive intermediates of "non-active" electrodes have yet to be fully elucidated[23]. These gaps raise critical questions: (1) Can single-atom-based EMSI effect serve as a powerful tool for enhancing efficient and selective •OH generation? (2) What is the underlying mechanism behind the enhanced EMSI effect by single-atoms during •OH generation? (3) Do the electrodes composed of low-cost transitional SACs hold significant potential for practical applications in EOPs?

Herein, we anchor different transition metals (Cu, Co, Ni) onto antimony-doped tin oxide (ATO, as a representative "non-active" anode) with highly tunable structures using magnetron sputtering technology to address the above questions. Notably, the Ni/ATO electrode presents remarkable electro-oxidation performance, promising application, and minimal environmental footprint in wastewater treatment. A comprehensive investigation into structural evolution and micro-interfacial mechanisms associated with the EMSI effect induced by atomically dispersed Ni species on ATO support is conducted, aiming to bridge the theoretical gaps between the EMSI effect and EOPs. This study confirms that the Ni single-atom-driven EMSI effect significantly enhances both adsorption and dissociation of interfacial H_2O molecules on Ni/ATO, while establishing rapid electron transfer channels to promote efficient and selective •OH generation. Importantly, Ni single-atoms act as co-catalytic sites through an "H-pulling effect" during •OH generation. The findings provide insights into the mechanism of coupling co-catalytic function with EMSI. Ultimately, this work offers strategies and theoretical perspectives for designing high-performance anodes, which is crucial for overcoming existing bottlenecks in EOPs.

Results

Electrocatalytic performance

The electro-oxidation activity of the prepared anodes was evaluated using sulfamethoxazole (SMX), an emerging pollutant commonly found in aquatic environments, as a model pollutant[26]. The sputtered layers of transition metals (Ni, Cu, or Co) were rapidly stripped within 5 min during pre-electrolysis under strong anodization, accompanied by voltage fluctuations (Supplementary Fig. 1a). Interestingly, both the cell voltage and catalytic activity of anodes tended to be stabilized following the removal of weakly bound metal components (Supplementary Fig. 1a, b). Among them, the Ni/ATO anode exhibited excellent electro-oxidation performance compared to other anodes (Fig. 1a), with negligible contributions from the cathode (Supplementary Fig. 1c). Specifically, SMX was completely degraded within 45 min in the Ni/ATO system, and its pseudo-first-order rate constant was ten-fold greater than that of bare ATO anode (Fig. 1b). Its performance surpasses that of most reported anodes (Supplementary Table 1), with a strong SMX mineralization capacity (Supplementary Fig. 2). Notably, the Ni/ATO anode achieved rapid and simultaneous removal of mixed pollutants including metronidazole (MNZ), ciprofloxacin (CIP), tetracycline (TC), 2,4-dichlorophenoxyacetic acid (2,4 D), atrazine (ATZ), and bisphenol A (BPA) (Fig. 1c). In contrast, sputtered metal-supported anodes without ATO support showed minimal pollutant degradation (Supplementary Fig. 3a), indicating that electrocatalytic performance is highly dependent on ATO presence. On this basis, the electrocatalytic activity can be regulated by adjusting the Ni loading on ATO support. As Ni loading increased, catalytic activity progressively enhanced up to a certain point (Fig. 1d and Supplementary Fig. 3b), but excessive deposition, causing nanoclusters aggregation or insufficient deposition resulting in active sites deficiency, diminished overall electrocatalytic performance. Therefore, a strong interaction between the ATO support and the supported Ni component significantly enhances electrocatalytic efficacy.

It is worth noting that a low current efficiency resulting from excessively high OER overpotential (such as in ATO) and the OER side reaction induced by insufficient overpotential (as observed in Co/ATO and Cu/ATO) impede •OH generation on the electrode surface[27]. Compared with other synthesized anodes, Ni/ATO exhibited a moderate OER overpotential along with a larger Tafel slope (Fig. 1e, f), which facilitated selective •OH production during EOPs[28]. Moreover, Ni/ATO presented the largest electrochemically active surface area (ECSA) and minimal charge transfer resistance (R_{ct}) (Fig. 1g and Supplementary Figs. 4, 5a), thereby providing sufficient active sites and enabling rapid charge transfer for electrocatalysis[29]. Additionally, there was a significant correlation between Ni loading levels and electrochemical activity. As Ni loading increased, the overpotential decreased towards the equilibrium potential for •OH generation (Fig. 1h)[30], improving current efficiency for •OH generation, however excessive loading resulted in elevated overpotentials. The anode with

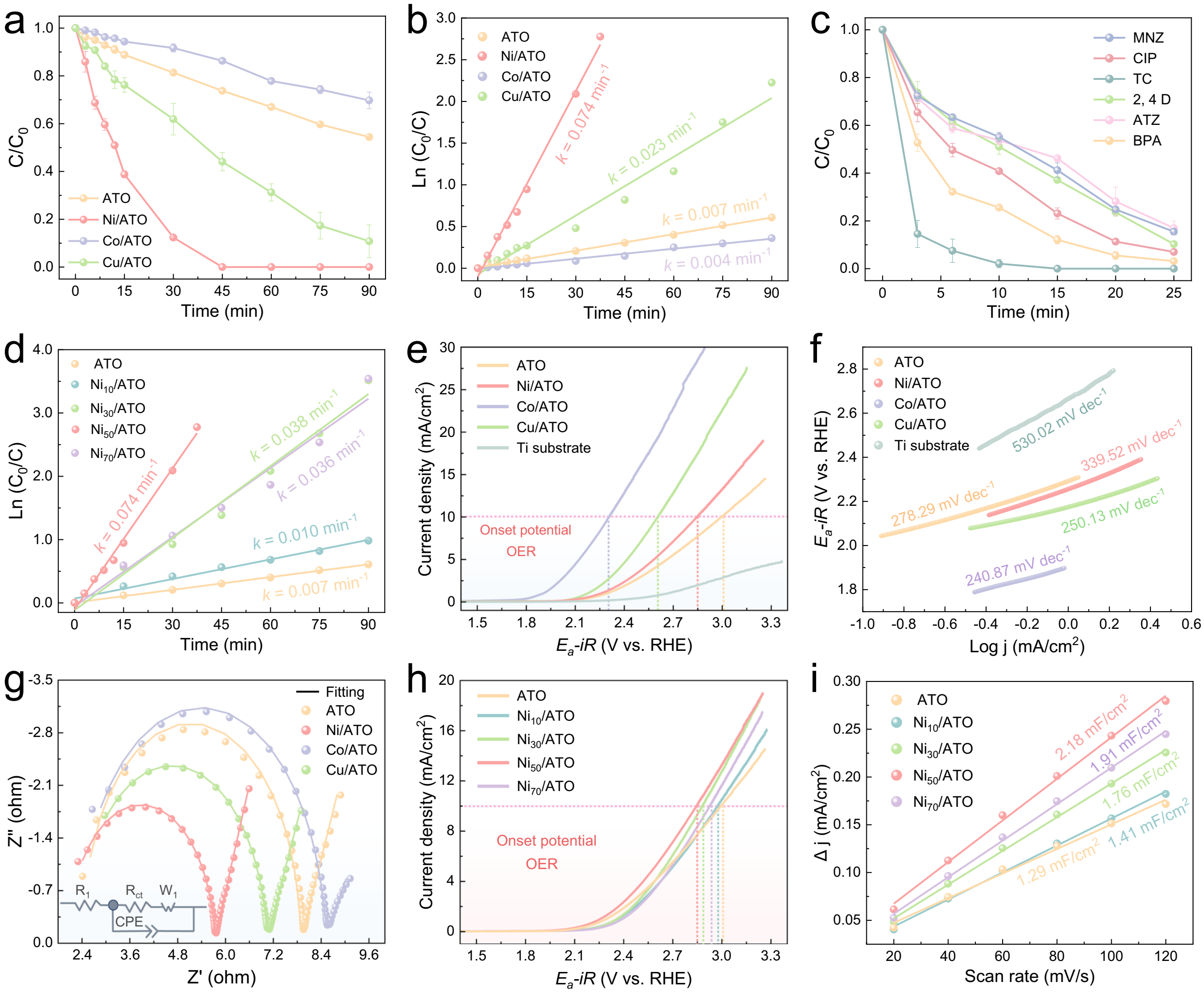

Fig. 1 | Electrocatalytic performance of electrodes. **a** Electro-oxidation performance of ATO anodes loaded with different transition metals for SMX degradation. **b** Corresponding first-order kinetic curves of (**a**). **c** Synchronous degradation performance of Ni/ATO electrode for various pollutants. **d** First-order kinetic curves corresponding to the electro-oxidation performance of Ni/ATO with different Ni loading. **e** LSV curves of ATO anodes loaded with different transition metals. **f** Corresponding Tafel plots of (**e**). **g** EIS Nyquist plots of ATO anodes loading with different transition metals, the inset showing the equivalent circuit. **h** LSV curves of Ni/ATO with different Ni loading. **i** ECSA of Ni/ATO with different Ni loading. In Ni_X/ATO (X = 10, 30, 50, 70), X refers to the deposition thickness of Ni (in nanometers) controlled by a quartz thickness gauge located in the sputtering chamber. Reaction conditions: [SMX] = 10 mg/L, [Na_2SO_4] = 50 mM, pH = 6.5, current density = 10 mA/cm² (in **a**–**d**), scan rate = 10 mV/s (in **e**, **f**, **h**), frequency range = 0.1–10^6 Hz, amplitude = 5 mV (in **g**), scan rates = 20–120 mV/s (in **i**). Experiments were conducted in triplicate, and the error bars represent the arithmetic mean ± standard deviation. Source data are provided as a Source Data file.

appropriate Ni loading (Ni_{50}/ATO) exhibited the smallest R_{ct} and the largest Tafel slope (Supplementary Fig. 5b, c). Furthermore, ECSA measurements and voltammetric charge results indicated that adequate Ni loading could furnish abundant active sites for ATO (Fig. 1i and Supplementary Figs. 6–8), promoting •OH generation and interfacial electron transfer processes. Therefore, the excellent electro-oxidation ability of ATO anode with appropriate Ni loading can be attributed to enhanced electrochemical activities.

Electrode characterizations

To thoroughly explore the structure-activity relationship of Ni/ATO, we conducted a systematic physicochemical characterization. The ATO catalytic layer, with an approximate 3.2 µm thickness, exhibited a dense porous structure composed of nanoparticles (~12.2 nm) (Fig. 2aI-II and Supplementary Fig. 9), thereby providing more active sites for electrochemical reactions. The sputtered Ni atoms underwent processes of adsorption, diffusion, and nucleation on the ATO surface to form nanoaggregates composed of Ni clusters (Fig. 2aIII and Supplementary Fig. 10)[31]. Interestingly, weakly bound Ni nanoparticles were detached during electro-oxidation in the pre-electrolysis, resulting in retained porous structure similar to that of ATO (Fig. 2aIV and Supplementary Fig. 11). Transmission electron microscopy (TEM) images further confirmed no significant morphological difference between Ni/ATO after pre-electrolysis and ATO (Supplementary Fig. 12). Energy dispersive X-ray spectroscopy (EDS) mapping showed uniform distribution of Ni, Sb, Sn, and O across the nanoscale electrode surface (Fig. 2b and Supplementary Fig. 13). Inductively coupled plasma-optical emission spectroscopy (ICP-OES) analysis indicated that Ni loading of the optimal sample (Ni_{50}/ATO) was 6.68 wt%, consistent with the EDS results (Supplementary Table 2). The X-ray diffraction (XRD) pattern showed that all diffraction peaks could be accurately assigned to the ATO solid solution, without any observable peak corresponding to metallic or oxidized Ni (Fig. 2c). Notably, elemental Ni peaks were detected from the electrodes prior to pre-electrolysis,

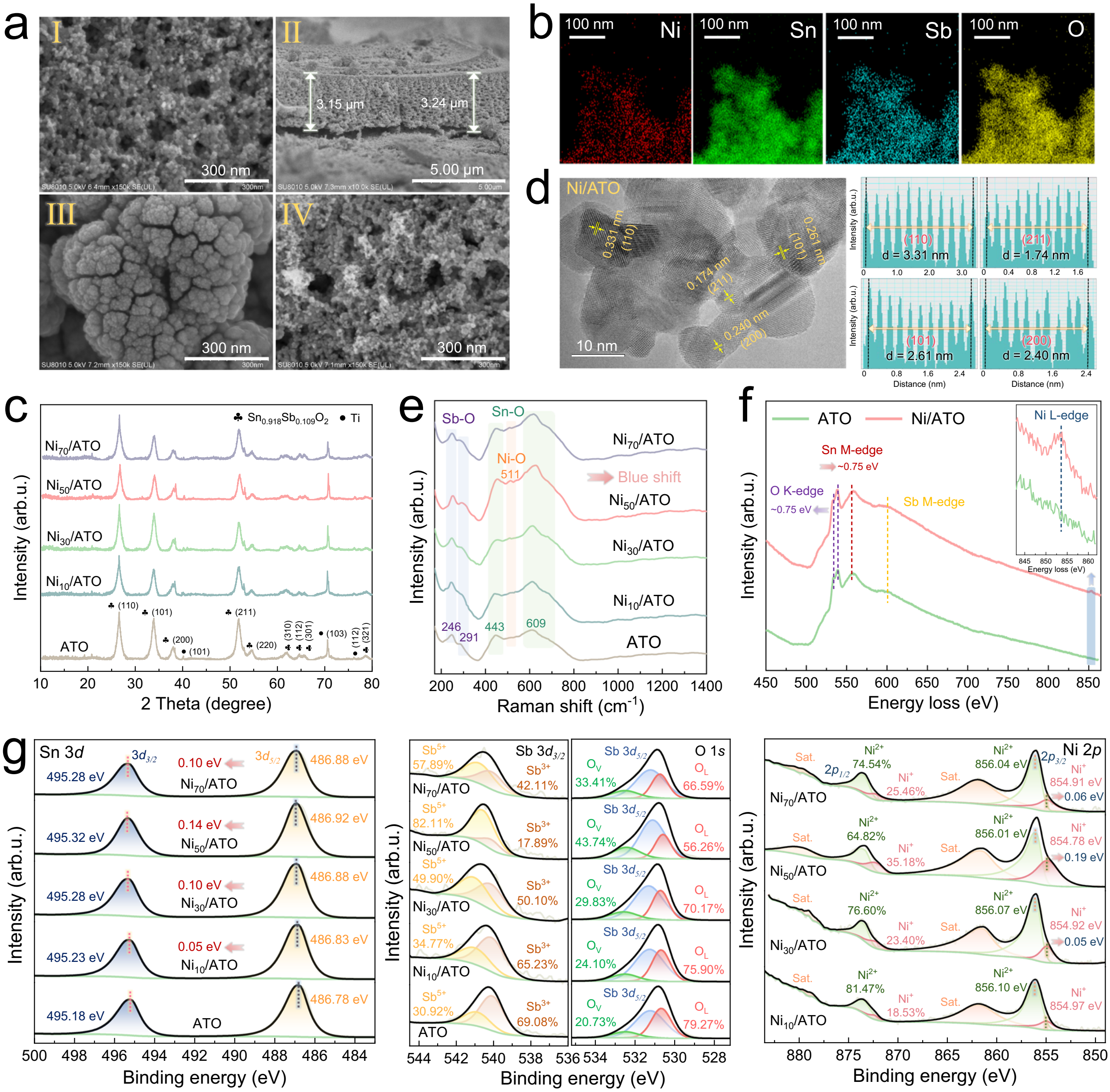

Fig. 2 | Structural characterizations of electrodes. a FESEM images of the ATO and Ni/ATO electrodes: I, II Surface and cross-sectional morphology of ATO electrode. III, IV Surface morphology of Ni/ATO without pre-electrolysis (III) and after pre-electrolysis (IV). **b** HRTEM-EDS elemental mapping images of Ni/ATO. **c** XRD patterns of ATO and Ni/ATO with different Ni loading. **d** HRTEM image and grayscale profile of Ni/ATO. **e** Raman spectra of ATO and Ni/ATO with different Ni loading. The distinct blue shift is evident in the Raman peak positions of the Ni_{50}/ATO relative to the pristine ATO. **f** EELS spectra of ATO and Ni/ATO. The purple and red arrows represent the shifts in the O K-edge and Sn M-edge peaks of Ni/ATO compared to ATO, respectively, and the inset figure pointed to by the blue arrow is a local enlargement of the blue shaded area. **g** XPS spectra with fitting curves of ATO and Ni/ATO with different Ni loading, including Sn 3*d*, Sb 3*d*, O 1*s*, and Ni 2*p*. O_L and O_V represent lattice oxygen and oxygen vacancies, respectively. Source data are provided as a Source Data file.

however, they disappeared after pre-electrolysis due to exfoliation effects on weakly bound Ni nanoparticles (Supplementary Fig. 14). Moreover, clear lattice fringes observed in high-resolution TEM (HRTEM) images are assigned to four primary crystal planes within ATO (Fig. 2d and Supplementary Fig. 15), indicating that loading of Ni did not alter the crystalline structure of ATO support, which aligns with the XRD results.

Raman spectra showed that a new peak corresponding to the vibration mode of Ni-O appeared following Ni deposition (Fig. 2e)[32], indicating coordination between Ni components and O atoms within ATO occurred upon Ni deposition. With optimal levels, the peak intensity related specifically to this interaction reached its zenith while exhibiting notable blue shifts, likely attributable to SMSI effects between the Ni component and ATO at an interface level[33]. Furthermore, electron energy loss spectroscopy (EELS) showed a new peak of Ni L-edge in Ni/ATO, alongside shifts at Sn M-edge towards higher energy and O K-edge towards lower energy (Fig. 2f), confirming electron transfer occurring from Sn atoms through O bridges into neighboring Ni atoms. Surface chemical states and electronic structures of the electrodes were analyzed via X-ray photoelectron spectroscopy (XPS). Relative contents of Ni diminished subsequent to pre-electrolysis, yet peak intensities tended to enhance with increasing loadings (Supplementary Fig. 16), indicating that trace Ni strongly bonded onto the ATO support may serve certain roles in enhancing overall oxidation capacities observed experimentally. As shown in Fig. 2g, the double peaks assigned to Sn^{4+} shifted to higher binding energy after Ni loading, which can be explained by the alterations induced by the aforementioned SMSI, leading to possible electron transfer originating from Sn to neighboring Ni domains[34]. Conversely, other metal-deposited electrodes showed negligible spectral shifts (Supplementary Fig. 17).

Ni has a larger surface energy and work function than the support, allowing electrons to transfer from the oxide with a higher Fermi level to the metal Ni with a lower Fermi level[34,35]. The SMSI effect thus enhances electrocatalytic performance by modulating the properties of the supports[15]. For example, supported Ni significantly raised the Sb^{5+}/Sb^{3+} ratio in ATO while reducing bandgap energy and suppressing carrier recombination (Fig. 2g and Supplementary Figs. 18, 19). This phenomenon can be explained by the enhanced charge transfer efficiency resulting from strong interactions within the Ni-O-Sn bond[36]. Meanwhile, the induced SMSI promoted the formation of oxygen vacancies, which are beneficial for improving the electrocatalytic ability[37]. As expected, these phenomena were not observed in electrodes dominated by weak metal-support interactions (Supplementary Figs. 20–22). Compared with a Ni/Ti without an ATO support, the Ni peak in Ni/ATO significantly shifted towards lower binding energy (Supplementary Fig. 23), attributable to the presence of the SMSI effect between Ni and ATO support. Following pre-electrolysis, weakly bound Ni components were stripped from the electrode surface, leading to the disappearance of metallic Ni^0 (Ni-Ni) while leaving only those Ni components bonded with surrounding O atoms. Interestingly, despite undergoing anodization, a relative content of Ni^+ increased with higher loading amounts and corresponding peaks shifted towards lower binding energy (Fig. 2g), which is attributed to the directional transfer of electrons towards Ni under the SMSI effect[34]. In contrast, excessive loading levels diminished active component formation due to nanoparticle-nanoparticle interactions to inhibit the SMSI effect[34,38].

Selective generation of active species and pollutant degradation mechanisms

Cyclic voltammetry (CV) experiments revealed no significant difference in the redox peaks of ferricyanide/ferrocyanide (Supplementary Fig. 24), and the current density did not exhibit a notable increase upon the addition of pollutants (Fig. 3a), thereby excluding the possibility of direct oxidation during pollutant degradation. Transient electro-generated active species were directly identified by electron spin resonance (ESR), with 5,5-dimethyl-1-pyrroline *N*-oxide (DMPO) and 2,2,6,6-tetramethyl-4-piperidone hydrochloride (TEMP) to capture •OH/$SO_4^{\bullet-}$ and singlet oxygen ($^1O_2$), respectively. Compared to other electrodes, the strongest signals of •OH, $SO_4^{\bullet-}$ and $^1O_2$ were detected in the Ni/ATO system (Fig. 3b and Supplementary Fig. 25), suggesting that its excellent electro-oxidation performance is attributed to the generation of the substantial active species (radicals and non-radicals). Quenching experiments were conducted to assess the contribution of these active species. The addition of high concentrations of tert-butyl alcohol (TBA, •OH quencher) or methanol (MeOH, •OH/$SO_4^{\bullet-}$ quencher) significantly inhibited SMX removal (Supplementary Fig. 26). •OH constituted 88.4% as the primary active species while $SO_4^{\bullet-}$ contributed only 2.5%, with slight contributions from both $^1O_2$ and direct oxidation at 9.1% (Fig. 3c).

It is worth noting that the inevitable non-selective quenching reactions and new radical chain reactions during quenching experiments may lead to misinterpretations of the reaction mechanism, which needs to be validated by combining multiple characterization techniques. Therefore, a chemical kinetic model encompassing adsorption, indirect oxidation involving radicals and non-radicals, alongside direct oxidation, was constructed based on probe experiments to validate the quenching results. The contributions by adsorption and cathodic oxidation could be disregarded (Supplementary Figs. 1c and 27a), and minimal abilities regarding direct oxidative processes were observed (Supplementary Fig. 27b). However, reaction kinetic constants of probe compounds within Ni/ATO (k_{NB}, k_{ATZ}, and k_{MNZ}) were significantly increased compared with other electrodes (Supplementary Figs. 28–30), substantiating indirect oxidation mechanisms driving electrocatalytic activities. As shown in Fig. 3d, e and Supplementary Fig. 31, •OH and $SO_4^{\bullet-}$ could be generated at consistent rates during the electrolysis, resulting in gradually increased exposure levels of the radicals. It is worth noting that steady-state concentrations of $[\bullet OH]_{SC}$ and $[SO_4^{\bullet-}]_{SC}$ in the Ni/ATO system improved by roughly fivefold and twofold, respectively. The $[\bullet OH]_{SC}$ was larger than $[SO_4^{\bullet-}]_{SC}$ exclusively in the Ni/ATO system, suggesting that Ni/ATO selectively generates •OH. Although elevated levels of $[^1O_2]_{SC}$ were detected in the Ni/ATO and Cu/ATO systems (Supplementary Fig. 32), $^1O_2$ is usually not a key active species in EOPs due to its relatively weaker oxidation property[39]. As shown in Fig. 3f, the kinetic constant of SMX degradation exhibited a significant linear positive correlation with $[\bullet OH]_{SC}$, while had no obvious correlation with $[SO_4^{\bullet-}]_{SC}$, thereby confirming that •OH predominantly drives pollutant degradation. Moreover, the relative contributions of active species to the degradation of emerging pollutants were evaluated based on the constructed chemical kinetic model (Supplementary Table 3). Compared with the Cu/ATO system, the relative contributions of •OH towards degrading various pollutants in the Ni/ATO system were the highest and showed selective enhancement, while contributions from direct oxidation and $^1O_2$ remained minimal without significant changes (Fig. 3g, h). Overall, radicals played a pivotal role in the EOP, while direct oxidation and $^1O_2$ contributed less due to mass transfer limitations and lower reaction rates between $^1O_2$ and organic pollutants[11,39].

In addition, computational kinetic modeling showed that both steady-state concentration and trends for active species generated during the electrocatalysis aligned closely with the above results (Supplementary Fig. 33). The highest steady-state concentration and reaction rate constants for •OH generation further confirmed that Ni/ATO electrode can selectively produce •OH (Supplementary Table 4). Moreover, reasonable regulation of Ni loading could optimize exposure levels as well as maintain a steady-state concentration of •OH, thereby achieving efficient electro-oxidation performance (Fig. 3i and Supplementary Figs. 34, 35).

Based on the main intermediates detected and the Fukui index results (Supplementary Fig. 36 and Tables 5, 6), four possible degradation pathways of SMX during electro-oxidation were proposed (Supplementary Fig. 37). Specifically, the corresponding sites of the SMX molecule were attacked by active species and underwent aniline oxidation/deamination, S-N/S-C bond cleavage, hydroxylation and ring-opening reactions to transform into intermediates with a smaller molecular weight, which were ultimately mineralized into inorganic salts, H_2O and CO_2. During the degradation process, the acute toxicity of intermediates gradually decreased, and the levels of developmental toxicity and bioaccumulation factor showed remarkable downward trends (Supplementary Fig. 38a–c). The toxicity test results from the *E. coli* culture also confirmed the gradual reduction of toxicity during the treatment of antibiotic wastewater by the Ni/ATO electro-oxidation system (Supplementary Figs. 38d, 39), which is crucial for improving water quality and reducing environmental risks.

Single-atom-driven EMSI effect and structural evolution

The aberration-corrected high-angle annular dark-field scanning TEM (AC HAADF-STEM) image clearly showed the atomic arrangement of Ni/ATO (Fig. 4a), and the brighter dots were attributed to overlapping Ni and Sn atoms based on atomic contrast difference[40,41]. As shown in Fig. 4b, c, the intensity profiles from both surface and line scans indicated that trace Ni was supported on ATO as isolated single-atoms. It was noteworthy that atomic-resolution elemental analysis revealed a

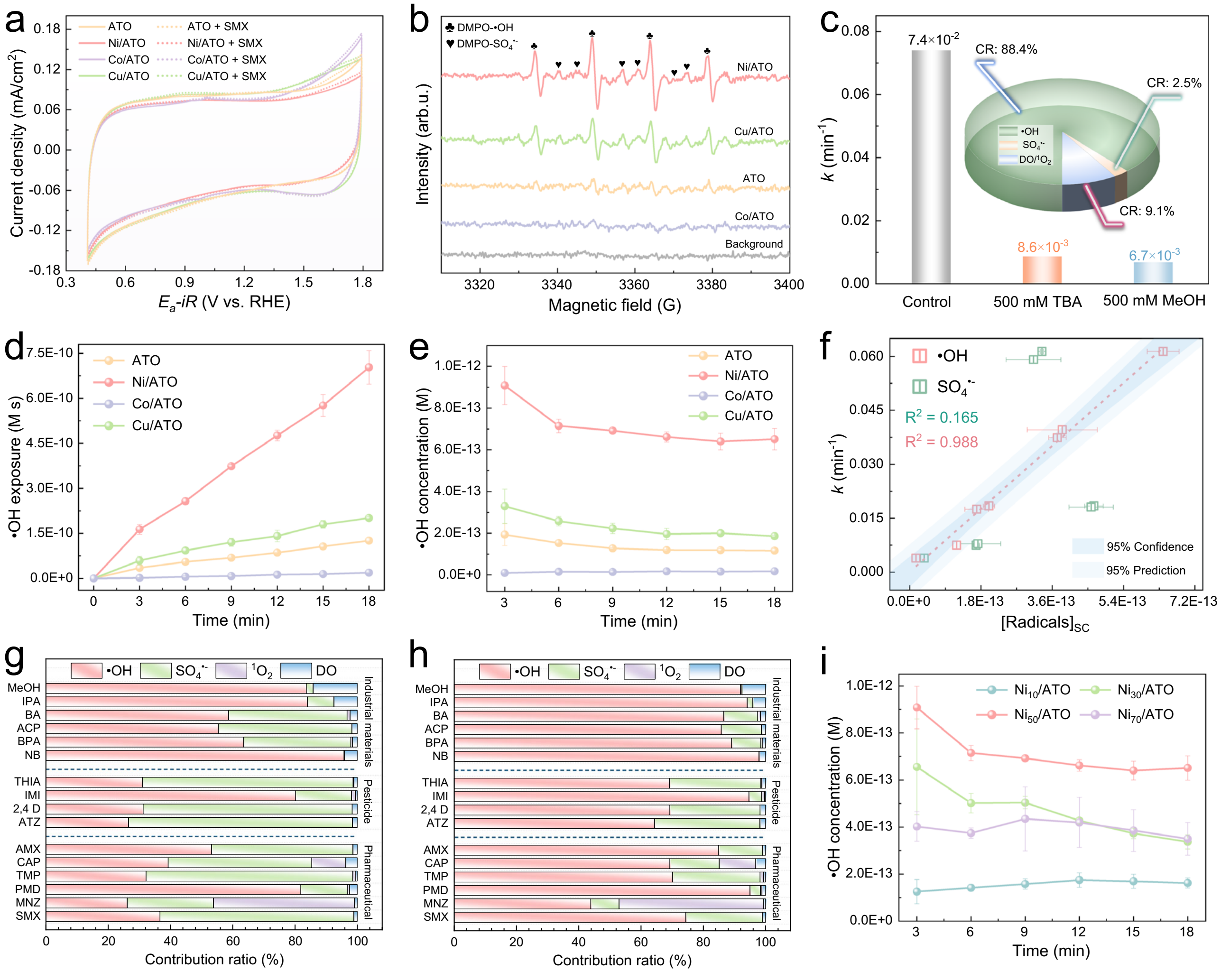

Fig. 3 | Efficient and selective •OH generation. **a** CV curves representing the direct oxidation effect of different electrodes. **b** ESR spectra using DMPO as a spin-trapping agent. **c** Pseudo-first-order rate constants for quenching experiments, the inset showing the contribution rates (CR) of active species and direct oxidation. **d**, **e** Exposure (**d**) and steady-state concentrations (**e**) of •OH in ATO anodes loading with different transition metals. **f** Correlation analysis between $[\text{Radicals}]_{SC}$ and the kinetic constant of SMX degradation. The 95% confidence reflects uncertainty in the regression line's mean estimate, while the 95% prediction reflects uncertainty in individual observations. **g**, **h** Contribution fraction of different active species/DO in the degradation of various pollutants by Cu/ATO system (**g**) and Ni/ATO system (**h**). IPA isopropanol, BA benzoic acid, ACP acetophenone, NB nitrobenzene, THIA thiacloprid, IMI imidacloprid, AMX amoxicillin, CAP chloramphenicol, TMP trimethoprim, PMD primidone. **i** Steady-state concentrations of •OH in Ni/ATO with different Ni loading anodes. Reaction conditions: $[Na_2SO_4] = 50$ mM, current density = 10 mA/cm² (in **a**–**i**), [SMX] = 10 mg/L (in **a**, **c**, **f**), scan rate = 50 mV/s (in **a**), [Quenchers] = 5–500 mM (in **c**), [Probes] = 8 μM (in **d**–**i**). Experiments were conducted in triplicate, and the error bars represent the arithmetic mean ± standard deviation. Source data are provided as a Source Data file.

uniform dispersion of Ni within the catalytic layer as individual atoms (Fig. 4d). In addition, the locally fine structure of the electrodes was studied by X-ray absorption spectroscopy (XAS). The Ni K-edge X-ray absorption near-edge structure (XANES) spectra presented that the absorption edge position of Ni/ATO was located between Ni foil and NiO (Fig. 4e), indicating that the valence state of Ni was between 0 and +2 (electron-rich), consistent with the XPS results. The K-space spectrum of Ni/ATO closely resembled that of the NiO reference (Supplementary Fig. 40), suggesting chemical coordination between Ni and O atoms[42]. As shown in Fig. 4f, Fourier transform extended X-ray absorption fine structure (EXAFS) spectra revealed structural peaks corresponding to strong Ni-O scattering (1.6 Å) in the first shell and weak Ni-O-Sn scattering (2.6 Å) in the second shell, and no contribution from Ni-Ni scattering (2.1 Å), thereby verifying that incorporated Ni exists as single-atoms dispersed throughout the ATO catalytic layer. The wavelet transform (WT) EXAFS spectra displayed only one intensity maximum assigned to the first-shell Ni-O scattering (Fig. 4g), reinforcing the evidence for dispersion of Ni single-atoms. Best-fit analysis from EXAFS showed that each Ni atom coordinated with approximately five O atoms, with an average bond length of ~2.05 Å (Fig. 4h and Supplementary Fig. 41), confirming that the oxidized state of Ni species is atomically dispersed on ATO. The detailed EXAFS fitting results are shown in Supplementary Table 7.

The SMSI effect driven by Ni single-atoms on the ATO support offers valuable insights into the EMSI effect in Ni/ATO, as it avoids the interference of the intrinsic metal effects[21]. As shown in Fig. 4i, the Sn K-edge XANES spectra indicate that the absorption edge position of Ni/ATO shifted to a higher energy, approaching that of the SnO_2 reference compared to ATO. This observation confirms a significant charge transfer from ATO to Ni single-atoms due to the EMSI effect, thereby altering the electronic state of Sn species, which was consistent with the XPS and EELS results. The EXAFS spectra showed that supported Ni single-atoms increased the Sn-O scattering (1.5 Å) intensity in the first shell, while markedly reducing the corresponding Sn-O-Sb/Ni scattering (3.5 Å) intensity (Fig. 4j). It was attributed to the slight structural changes resulting from bonding interactions between Ni single-atoms

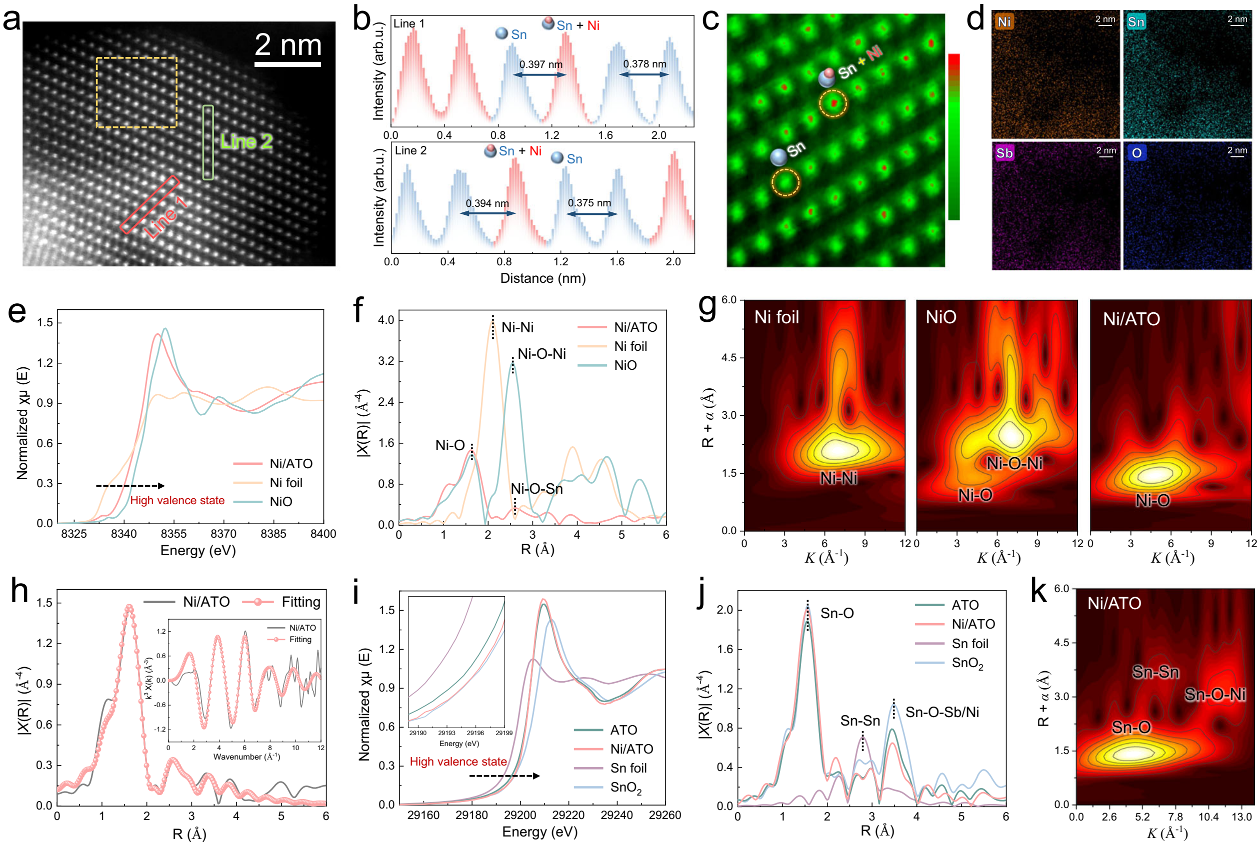

Fig. 4 | Single-atom-driven EMSI effect. a AC HAADF-STEM image of Ni/ATO. **b** Corresponding line intensity profiles. **c** Corresponding surface intensity profile. The region corresponds to the area highlighted by the yellow dashed box in (**a**). The red and green in the color scale represent high signal intensity and low signal intensity, respectively. **d** HAADF-STEM-EDS elemental mapping images. **e** Ni K-edge XANES spectra of Ni foil, NiO, and Ni/ATO. **f** Corresponding Fourier transform Ni K-edge EXAFS spectra. **g** Corresponding wavelet transform (WT) EXAFS spectra. The bright yellow and dark red areas in the (**g**, **k**) represent high signal intensity and low signal intensity, respectively. **h** Ni K-edge EXAFS best-fit analysis of Ni/ATO in R space and k space (inset). **i** Sn K-edge XANES spectra of Sn foil, SnO_2, ATO, and Ni/ATO, the inset showing the partial enlargement of the pre-edge peak. **j** Corresponding Fourier transform Sn K-edge EXAFS spectra. **k** WT-EXAFS spectra of Ni/ATO. Source data are provided as a Source Data file.

and O atoms in the support. After loading with Ni single-atoms, there was a notable alteration in the coordination environment of the electrocatalyst (Supplementary Figs. 42–44 and Table 8), which was attributed to the electronic feedback from Sn to Ni arising from the EMSI effect[16]. Similarly, an analysis of the WT-EXAFS spectra corroborated these findings (Fig. 4k and Supplementary Fig. 45).

Theoretically, the sputtered Ni atoms, affected by free energy and the equilibrium concentration, will diffuse and migrate longitudinally inside the porous catalytic layer[31]. As shown in Fig. 5aI-II, Ni nanoaggregates were still detected at a longitudinal distance of ~440 nm in the catalytic layer without pre-electrolysis, significantly exceeding the 50 nm limit imposed by the thickness gauge, thereby verifying the migration and aggregation of Ni atoms deep into the ATO support. Following pre-electrolysis, both surface and internal Ni nanoaggregates within the catalytic layer were completely removed (Supplementary Fig. 46). In addition, cross-sectional EDS displayed uniformly distributed Ni throughout the entire porous structure of Ni/ATO (Supplementary Fig. 47), indicating that sputtered Ni single-atoms can diffuse into various corners of this porous architecture. In contrast, weakly bound Ni components were immobilized on ATO through annealing treatment to explore the key roles of the Ni single-atom-driven EMSI effect during EOP.

Results showed a sharp decline in electro-oxidation ability for the annealing-treated Ni/ATO under different atmospheres, and this reduction correlated strongly with Ni loading levels (Supplementary Fig. 48). This phenomenon may be due to aggregation and nucleation of undetached Ni clusters covering single-atom sites. SEM, XRD, and HRTEM revealed that numerous NiO nanoparticles (~35.3 nm) formed throughout the entire porous catalytic layer after the annealing treatment (Fig. 5aIII-IV and Supplementary Figs. 49–52), leading to the diminished capacity for •OH generation (Fig. 5b, c and Supplementary Fig. 53). It was worth noting that prolonged anodization resulted in these NiO nanoparticles stripped away while restoring electrode morphology to a porous structure composed primarily of ATO nanoparticles (~12.5 nm) (Fig. 5aV-VI and Supplementary Figs. 51, 54). Interestingly, as the exfoliation of NiO alongside the re-exposure of Ni single-atoms, the electro-oxidation capacity of the electrode gradually improved to a level comparable to that of Ni/ATO without annealing treatment (Fig. 5d). The electrochemical characterization and XPS results indicate that the concealment of Ni single-atom sites leads to severe OER side reaction and a marked decrease in the number of active sites and charge transfer capacity at the anodes (Supplementary Figs. 55–59). With the re-exposure of Ni single-atoms, both electrochemical activity and •OH generation were recovered. Therefore, limitations imposed by migration of Ni single-atoms into the catalytic layer considerably diminished its electro-oxidation ability (Supplementary Fig. 60). Similarly, a reduction in active sites correlated with decreased electrochemical activity for •OH generation (Supplementary Figs. 61–63).

The EMSI effect triggered by Ni single-atoms on ATO played a crucial role in improving electro-oxidation performance and electrode stability. Based on the aforementioned experimental and

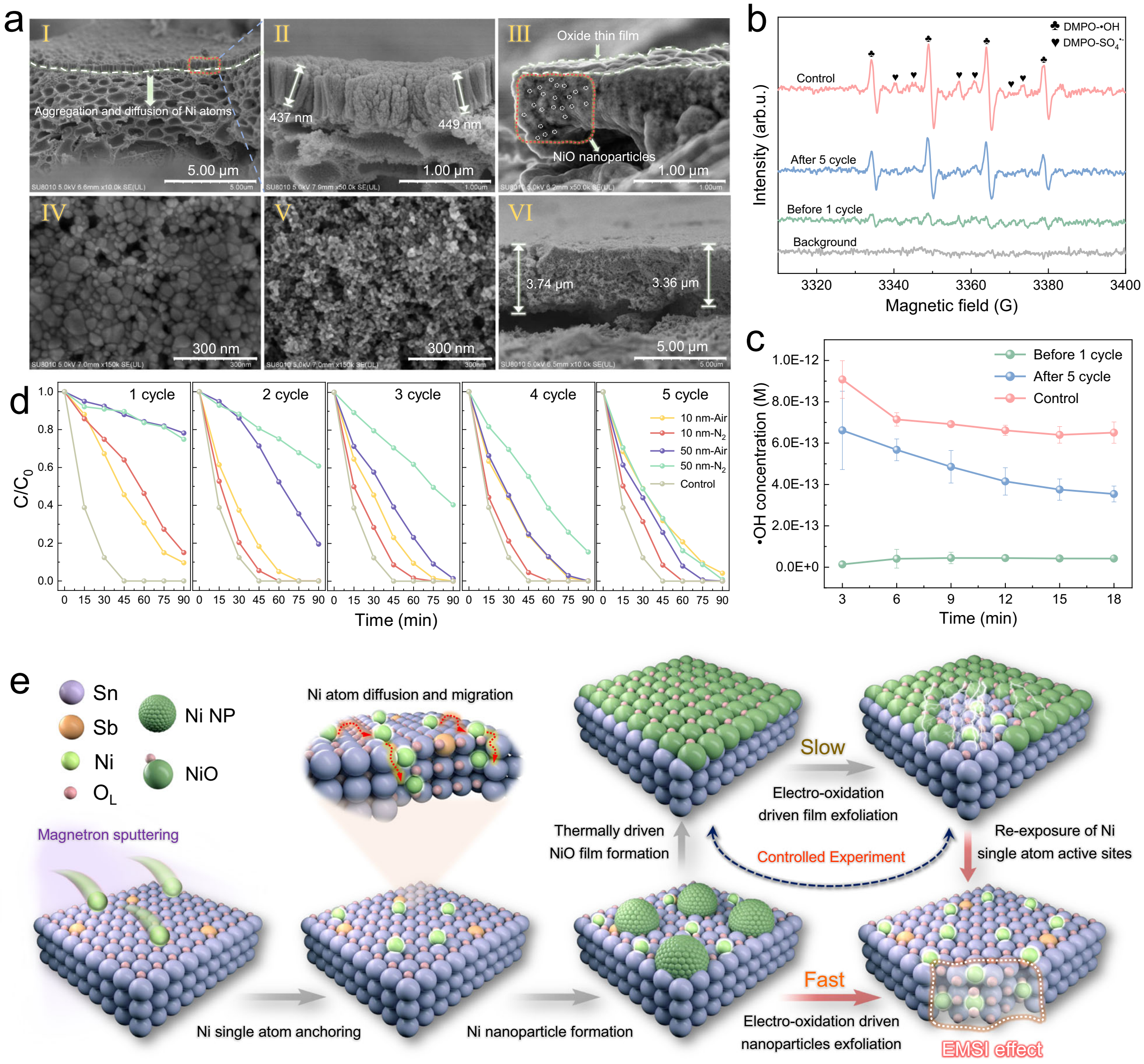

Fig. 5 | Structural evolution process based on the EMSI effect. **a** FESEM images of Ni/ATO after annealing treatment and cycling experiments: Cross-sectional morphology of Ni/ATO without annealing and pre-electrolysis (I, II) and annealing-treated Ni/ATO (III). IV Surface morphology of annealing-treated Ni/ATO. Surface (V) and Cross-sectional (VI) morphology of annealing-treated Ni/ATO after cycling experiments. **b**, **c** ESR spectra (**b**) and •OH steady-state concentrations (**c**) of Ni/ATO after annealing treatment (before 1 cycle) and cycling experiments (after five cycles). **d** Cycling experiments of annealing-treated Ni/ATO on SMX degradation. **e** Structural evolution process of single-atom-driven EMSI effect, the sputtered Ni atoms undergo adsorption, diffusion, migration, and are ultimately anchored in single-atom form inside the ATO support. Unless otherwise specified, annealing treatment was carried out in an air atmosphere. Reaction conditions: [Na_2SO_4] = 50 mM, current density = 10 mA/cm^2 (in **b**–**d**), [Probes] = 8 μM (in **c**), [SMX] = 10 mg/L, pH = 6.5 (in **d**). Experiments were conducted in triplicate, and the error bars represent the arithmetic mean ± standard deviation. Source data are provided as a Source Data file.

characterization results, the structural evolution of the Ni/ATO was illustrated (Fig. 5e). Specifically, Ni atoms were initially deposited on the ATO surface under high-speed ion beam bombardment, where Ni atoms with appropriate energy will adsorb on the ATO support. Subsequently, these Ni single-atoms diffused and migrated longitudinally throughout the entire catalytic layer in search of stable binding sites, becoming anchored through coordination with O atoms to establish the EMSI effect[31]. Meanwhile, a major fraction of Ni single-atoms underwent local collisions and aggregated into atomic clusters that gradually evolved into nano-islands. Notably, pre-electrolysis quickly and effectively removes weakly bound Ni nanoparticles/clusters while remaining and exposing strongly bound Ni single-atoms, and this process allows for the exertion of the EMSI effect to enhance electrocatalytic performance. However, the covering of Ni single-atoms can severely inhibit the EMSI effect and reduce catalytic activity. Control experiments involving annealing treatment further verified that the EMSI effect was indeed driven by these Ni single-atoms.

Exploration of electrocatalytic mechanism

In situ electrochemical Raman analysis was used to reveal the dynamic alterations in the intrinsic structure and adsorbed species on the electrode during electrocatalysis. Despite signal attenuation caused by the solution layer, distinct variations in Raman peaks were observed under the influence of the EMSI effect (Supplementary Fig. 64). As shown in Fig. 6a and Supplementary Fig. 65, the intensity of the Raman peaks corresponding to Sn-O vibrations on the ATO electrode progressively diminished with increased applied potential, probably because O_2 produced from side reactions hindered the signals[32].

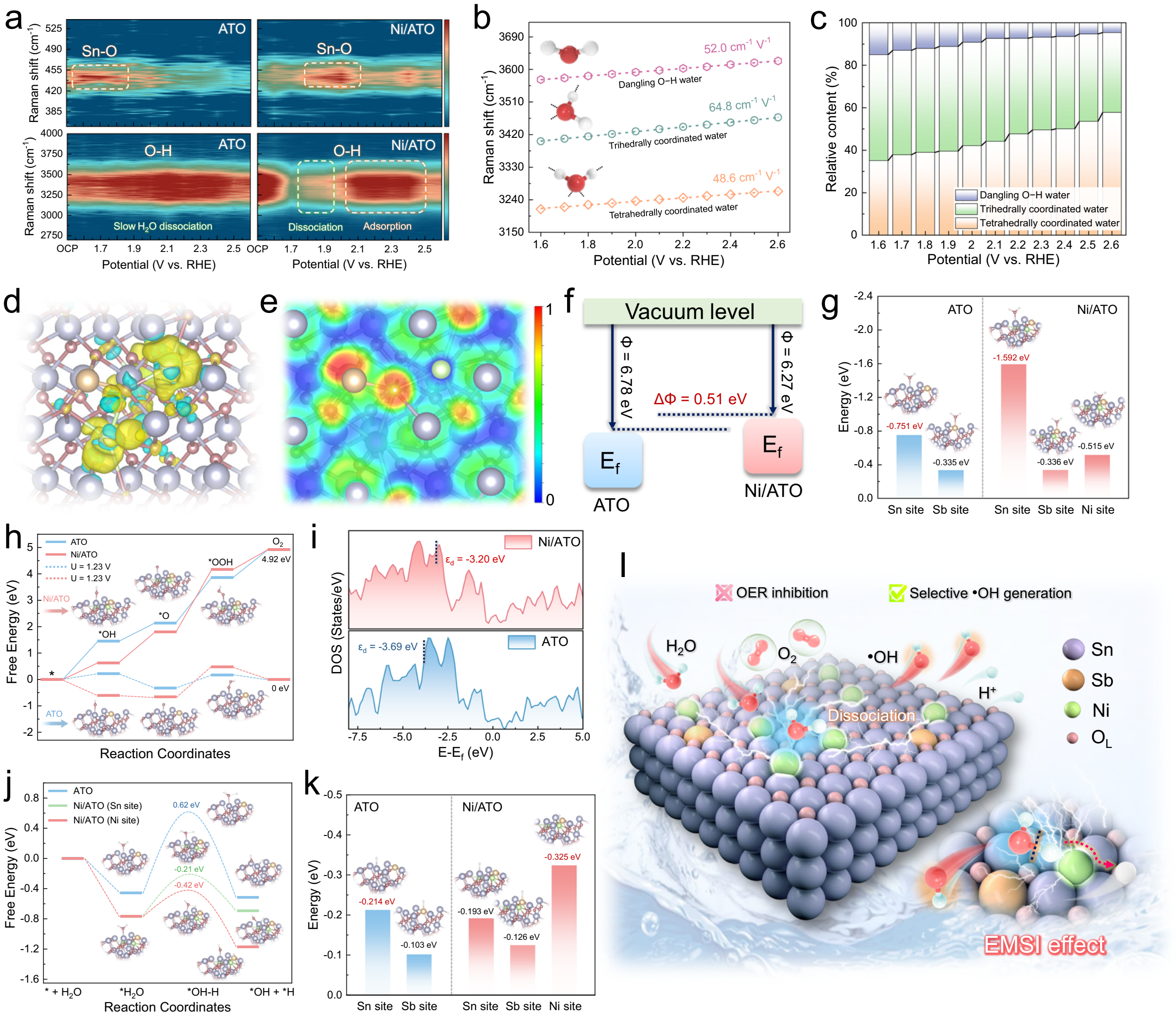

Fig. 6 | Micro-interface mechanisms of electrocatalysis. **a** Mapping of in situ Raman spectra of ATO and Ni/ATO at corresponding Sn-O and O-H vibration modes. The red and blue in the color scale represent high signal intensity and low signal intensity, respectively. **b** Frequency plot of changes in the O−H in Raman spectra of different coordinated waters at Ni/ATO surface. **c** Variation of the relative contents of differently coordinated water on the Ni/ATO surface with applied potential. **d** Differential charge density of Ni/ATO. The blue and yellow isosurfaces refer to charge depletion and accumulation, respectively. **e** The electron localization function of Ni/ATO. **f** Schematic illustration of the work functions of ATO and Ni/ATO. **g** Energy of water molecule adsorption at different sites on ATO and Ni/ATO. **h** Free-energy diagram for OER of ATO and Ni/ATO. **i** Total DOS of ATO and Ni/ATO. **j** Energy barriers for water dissociation at different H adsorption sites on ATO and Ni/ATO. **k** Energy of H adsorption at different sites on ATO and Ni/ATO after water dissociation. **l** Micro-interface mechanisms of Ni single-atoms driven EMSI in selective •OH generation. All atoms in the models are the same as those listed in **l**. Source data are provided as a Source Data file.

Interestingly, for Ni/ATO, the Sn-O vibration peaks initially intensified as applied potential increased, indicating continuous dissociation of H_2O molecules into *OH[43,44]. When applied potential exceeded 2.1 V (vs. RHE), conversion of adsorbed intermediates occurred with a decline in Raman signals, and this phenomenon correlated with a high overpotential of Ni/ATO approaching equilibrium potential for •OH production[30]. Therefore, the EMSI effect promotes direct generation of •OH while diminishing OER activity.

To further investigate the selective •OH generation process, we studied both structural dynamics and behavior of H_2O molecules at the solid-liquid interface[45]. The interfacial water's O-H stretching vibration intensity on Ni/ATO surpassed that on ATO, implying stronger interactions with H_2O molecules (Supplementary Fig. 66)[46]. Furthermore, curve fitting revealed three Gaussian peaks corresponding to different coordination modes: dangling O−H water (~3600 cm^{-1}), trihedrally coordinated water (~3400 cm^{-1}), and tetrahedrally coordinated water (~3200 cm^{-1}) (Supplementary Fig. 67)[46]. Due to Stark tuning effects from surface adsorbed species[47], central Raman peaks related to these coordination modes exhibited blue shifts as the applied potential increased. Notably, Ni/ATO displayed significantly higher Stark slopes than ATO (Fig. 6b and Supplementary Fig. 68). It is further indicated that strong interactions between the electrocatalyst and interfacial water facilitate disruption of O−H bonds within adsorbed H_2O[46,48]. In comparison to ATO (Supplementary Fig. 69), modifications in electronic structure within Ni/ATO led to transformation of adsorbed interfacial water into a highly ordered tetrahedrally coordinated form (Fig. 6c)[49], which is beneficial for optimizing electrochemical energy conversion[12]. Meanwhile, frequency and intensity changes among interfacial water peaks on Ni/ATO showed heightened dependence on applied potential (Fig. 6a), indicating enhanced electron transfer efficiency during the dissociation processes involving interfacial H_2O[48]. The dynamic transitions observed in H-O-H and O-H stretching vibrations confirmed rapid dissociation and re-adsorption cycles occurring among interfacial water molecules on Ni/ATO, providing sufficient active sites for selective •OH generation (Supplementary Fig. 70).

To comprehensively reveal the structure-performance relationship of Ni/ATO and clarify the critical role of the EMSI effect in enhancing catalytic activity, we conducted extensive density functional theory (DFT) calculations. Based on characterization results, corresponding theoretical models for ATO and Ni/ATO were constructed. Compared to the doping mode, Ni loading mode coordinated with five O atoms exhibited the lowest formation energy (Supplementary Fig. 71), consistent with the EXAFS results. As shown in Fig. 6d, differential charge density analysis reveals that the EMSI effect triggered charge redistribution on the ATO surface, characterized by notable charge accumulation around Ni atoms at a transfer amount of 0.29 e^-. It indicates a strong electronic interaction between Ni single-atoms and the ATO support, confirming directional electron transfer from the ATO support to Ni single-atoms induced by the EMSI effect[29], corroborated by XPS, EELS, and XANES. Under the EMSI influence, Ni/ATO exhibited markedly enhanced electronic delocalization as revealed by electron localization function analysis (Fig. 6e and Supplementary Fig. 72), along with a substantial reduction in work function to 6.27 eV (Fig. 6f), signifying an increase in active electrons and enhanced electron transfer efficiency[50,51]. The formation of Sn–O–Ni bonds may trigger quantum spin-exchange interactions to establish rapid electron transport channels within the catalytic layer, facilitating efficient charge transfer[52]. Additionally, partial density of states (PDOS) showed that the loading of Ni single-atoms significantly enhanced hybridization among metal atomic orbitals (Supplementary Fig. 73), thereby optimizing electronic structure within Ni/ATO through strong electron transfer[51].

The adsorption capacities of different sites for H_2O molecules and *OH were assessed (Fig. 6g and Supplementary Fig. 74). The results showed that electron-deficient Sn atoms served as the preferred adsorption sites for H_2O molecules rather than Ni or Sb atoms. Compared to ATO, Ni/ATO exhibited a higher H_2O adsorption energy (−1.592 eV), indicating that loading of Ni single-atoms significantly improved the adsorption capacity of H_2O molecules on the electrode surface. Thermodynamic calculations of the four elementary electron steps in OER revealed that the energy barrier for *OH generation on Ni/ATO was considerably lower than that on ATO, suggesting a greater propensity for *OH generation during electrolysis (Fig. 6h). Conversely, Ni/ATO exhibited a higher barrier in the rate-determining step of OER, consistent with its reduced activity in OER side reaction observed experimentally. Similarly, the shift of the d-band center (ε_d) of Ni/ATO toward the Fermi level led to enhanced adsorption energy between the electrode surface and intermediate species (Fig. 6i)[53], which was unfavorable for OER. Additionally, Bader charge analysis indicated that Ni/ATO displayed a greater amount of charge transfer after *OH generation (Supplementary Fig. 75), validating significant enhancements in electron transfer efficiency under the EMSI effects. XPS further confirmed the efficient electron transfer process among different metal sites during electrolysis (Supplementary Fig. 76).

From a kinetic perspective, the kinetic energy barrier for H_2O dissociation on Ni/ATO was substantially lower than that on ATO (Fig. 6j). The Sn sites and Ni single-atom sites exhibited strong adsorption capabilities for H_2O molecules and *H species, respectively (Fig. 6k). Interestingly, when Ni single-atom acting as an adsorption site for *H following OH-H bond cleavage, the kinetic energy barrier for H_2O dissociation was further reduced, consistent with the in situ Raman results. This suggested that the OH-H bond of H_2O adsorbed at Sn sites achieved enhanced dissociation efficiency through the "H-pulling effect" from electron-rich Ni sites, thus highlighting synergistic roles of these single-atoms as "co-catalytic" entities in favoring selective generation of •OH[23]. In summary, EMSI effects driven by Ni single-atoms not only significantly enhanced both adsorption and dissociation capacities of H_2O molecules but also established rapid electron transfer channels for promoting the selective •OH generation, thereby substantially improving overall catalytic performance (Fig. 6l).

Feasibility of practical application and environmental footprint

The stability, adaptability, manufacturing, and operating costs of the electrode are key indicators for assessing its potential applications. The cyclic experiments showed that the electro-oxidation performance of Ni/ATO was highly stable (Fig. 7a). The concentration of metal ions in leakage was minimal and fully complied with industrial wastewater discharge standards of China (Supplementary Fig. 77), suggesting that Ni/ATO posed no potential ecological risk. Characterizations further validated the structural stability of Ni/ATO (Supplementary Fig. 78). Furthermore, electrode adaptability was evaluated through adjustments in water quality and operating conditions, energy consumption calculations, and real wastewater treatment. Due to its high •OH generation capacity, the Ni/ATO-based EOP effectively removed various emerging pollutants, including antibiotics, pesticides, and industrial raw materials (Fig. 1c). Despite •OH's lower oxidation potential in alkaline water, organic pollutants were still rapidly eliminated across a broad pH range (3 ~ 11) (Supplementary Fig. 79a, b). While high concentrations of HCO_3^- and NO_3^- slightly diminished electro-oxidation efficiency due to anionic quenching effects on •OH, the degradation efficiency significantly improved in the presence of Cl^- (Supplementary Fig. 80a, b). Quenching experiments confirmed that •OH was an essential active species (Supplementary Fig. 80c, d), suggesting that enhanced electro-oxidation performance might be attributed to chlorine radical generation mediated by •OH[54]. Moreover, complex ions and organic matters in real water matrices, including lake, river, and tap water slightly reduced SMX degradation performance (Supplementary Fig. 79c, d and Table 9), however, the Ni/ATO-based EOP exhibited robust anti-interference capabilities. A judiciously maintained current density facilitated •OH production, thereby improving SMX removal efficiency and reducing operational energy consumption (Supplementary Fig. 81). The Ni/ATO anode exhibited the lowest operational energy consumption compared with other prepared and reported anodes (Supplementary Fig. 82 and Table 10).

The feasibility for real antibiotic wastewater treatment was evaluated without adding any auxiliary electrolytes, considering the high salinity of industrial wastewater (Supplementary Table 11). After a 2 h treatment, the wastewater became clear and transparent, achieving complete decolorization (Fig. 7b). The 3D excitation-emission matrix (3D-EEM) fluorescence spectrum showed that the main components of antibiotic wastewater were non-biodegradable humic acid-like substances (Supplementary Table 12). As shown in Fig. 7c and Supplementary Figs. 83, 84, the fluorescence range gradually narrowed during the electro-oxidation, while central fluorescence intensity initially increased within 40 min before rapidly declining. This phenomenon can be attributed to the preferential degradation of high molecular weight humic acid-like substances into small molecular organic matters that accumulated during the initial stage of treatment, and complete degradation was subsequently achieved through continuous electrolysis in later stages. In comparison with ATO, Ni/ATO successfully accomplished a total removal of humic acid-like substances within 2 h. Correspondingly, the Ni/ATO-based EOP presented superior efficiency in wastewater treatment, with UV_{254} and total organic carbon (TOC) removal rates reaching 76.7 and 64.8%, respectively (Fig. 7d). Notably, energy consumption for treating real antibiotic wastewater using the Ni/ATO-based EOP was only 0.05 kWh/g TOC, which was significantly lower than previously reported values (Fig. 7e and Supplementary Table 10). These results indicate that sustained generation of •OH facilitated by Ni/ATO contributes to maintaining relatively constant energy consumption levels throughout EOP.

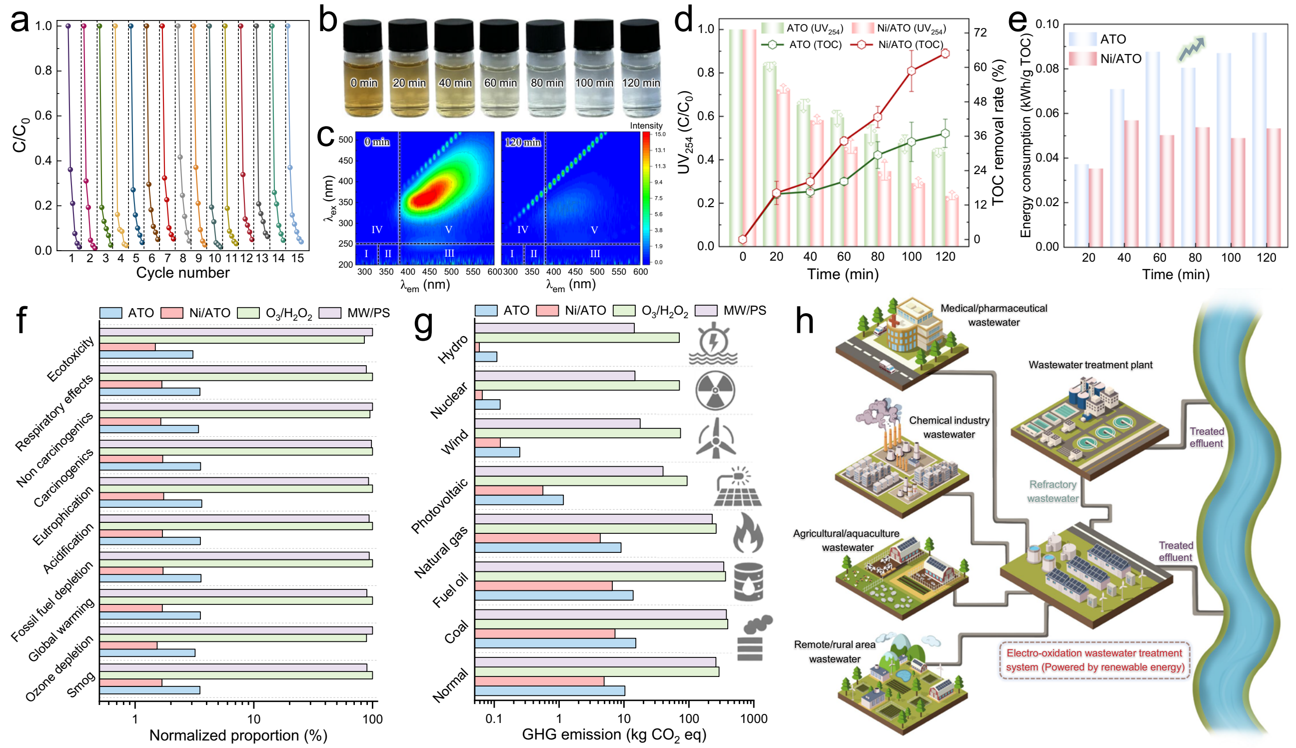

Fig. 7 | Practical application potential and environmental footprint. **a** Cyclic experiment of SMX removal by the Ni/ATO. **b** Decolorization performance of Ni/ATO in treating real pharmaceutical wastewater. **c** 3D-EEM fluorescence spectra of Ni/ATO in treating real pharmaceutical wastewater. The I, II, III, IV, and V regions represent aromatic proteins I, aromatic proteins II, fulvic acid-like, soluble microbial metabolites, and humic acid-like, respectively. **d**, **e** Decontamination effect (**d**) and operational energy consumption (**e**) of electro-oxidation treatment on pharmaceutical wastewater. **f** Impact scores of all environmentally relevant descriptors in ATO, Ni/ATO-based EOP, and common homogeneous advanced-oxidation. **g** GHG emission for ATO, Ni/ATO-based EOP and common homogeneous advanced-oxidation using electricity from different sources. **h** Promising application scenarios for treating various wastewater through Ni/ATO electro-oxidation system powered by renewable energy. Experiments were conducted in triplicate, and the error bars represent the arithmetic mean ± standard deviation. Source data are provided as a Source Data file.

Furthermore, it is estimated that the cost associated with Ni/ATO fabrication is as low as 0.25 RMB/cm^2, and the construction of the single-atom-induced EMSI effect only increases the manufacturing cost by ~20%. This remains significantly lower than the price of commercial electrodes (Supplementary Fig. 85).

The environmental carbon footprint and overall environmental impacts of EOPs and common homogeneous advanced-oxidation systems were analyzed through a life-cycle assessment (LCA). Compared to the ATO-based EOP, which has an emission of 10.3 kg CO_2 equivalent, the Ni/ATO-based EOP demonstrated a significant reduction in greenhouse gas (GHG) emissions to 4.9 kg CO_2 equivalent within a 95% confidence interval (Supplementary Table 13). Notably, due to lower energy input and the absence of chemical agents, GHG emissions from the ATO-based EOP are substantially lower than those from homogeneous oxidation processes, such as O_3/H_2O_2 and microwave/persulfate (MW/PS) (Fig. 7f). Additionally, the Ni/ATO-based EOP exhibited the minimal environmental impacts concerning resource consumption, ecosystem and human health. However, reliance on conventional fossil fuels results in increased GHG emissions and associated overall environmental impacts, nonetheless, environmental loads remain significantly lower than those observed in homogeneous oxidation systems (Fig. 7g and Supplementary Table 14). Conversely, with advancements in renewable energy sources (wind, photovoltaic, nuclear, hydro), the GHG emissions from the Ni/ATO system could be further reduced by over 85%, alongside a marked decrease in overall environmental impacts. Considering potential industrial-scale implementation, where resource utilization can be maximized, the environmental impacts would be significantly minimized. Importantly, the Ni/ATO-based EOP, with its exceptional catalytic oxidation capabilities and low environmental carbon footprint, provides a robust technical support for future integrated wastewater treatments (Fig. 7h). For example, coupling this system with electrodialysis could achieve dual objectives of wastewater decontamination and chemical recovery[55], thereby supporting the realization of carbon neutrality goals.

Discussion

In this study, we conducted a comprehensive and systematic exploration of the structural evolution process and micro-interface mechanisms associated with the EMSI effect induced by atomically dispersed Ni species on the ATO support, addressing the limitation of conventional SMSI effect regarding active site exposure and electron transfer efficiency. By regulating the electronic structure, the EMSI effect significantly enhanced the adsorption and dissociation efficiency of H_2O molecules during electro-oxidation, along with improving electron transfer efficiency. This study revealed the "H-pulling effect" of Ni single-atoms as co-catalytic sites, emphasizing their pivotal role in •OH generation. The superior electrocatalytic activity could be achieved by precisely regulating the dispersed atomic states of Ni, effectively avoiding the OER side reaction. The Ni/ATO anode exhibited great electrocatalytic performance and applicability in the degradation of various refractory pollutants. In real wastewater treatment, the EOP based on Ni/ATO achieved high-efficiency water decontamination within 2 h (~65% TOC removal) and low operational energy consumption (0.05 kWh/g TOC) without additional electrolytes. Furthermore, the LCA analysis showed that the EOP based on Ni/ATO had a lower environmental footprint compared to homogeneous oxidation processes. In summary, this work not only highlights the potential of single-atom-driven EMSI effect in improving electrochemical catalytic performance, but also provides a robust technological solution for wastewater purification.

Methods

Chemicals

All chemicals were of an analytical grade and used as received without further purification, unless otherwise specified. A complete list is provided in Supplementary Methods. Ultrapure water with a resistivity of 18.2 MΩ•cm was used for solution preparation.

Synthesis of ATO and Ni/ATO electrodes

ATO electrodes were synthesized by an impregnation-calcination method. Specifically, Ti substrates were polished with sandpaper and degreased by ultrasonic treatment in acetone, ethanol, and ultrapure water, subsequently. The treated Ti substrates were etched in a slightly boiling 10 wt% oxalic acid solution for 45 min, and then were immersed in the prepared ATO precursor solution (0.45 M Sn^{4+} and 0.02 M Sb^{3+} in isopropanol) for 30 s. The impregnated substrates were dried at 85 °C and then annealed at 550 °C for 5 min to form an ATO catalytic layer in situ. After ten cycles of impregnation and annealing, the preparation of the ATO electrode was finally completed by annealing at 550 °C for 1 h.

Ni/ATO electrodes (2×2 cm^2) were prepared by a confocal magnetron sputtering system (VTC-600-2HD, China) equipped with a DC power supply. The accelerated argon ions collide elastically with a high-purity Ni target (99.99%), depositing Ni atoms on the supported ATO electrodes. ATO electrodes were placed on a rotating and heated turntable (10 rpm, 150 °C) to ensure uniform loading of metal atoms. Ultrapure argon (30 mL/min) was used as the sputtering gas to provide a working pressure of 5.4×10^{-2} hPa. After pre-sputtering for 2 min, Ni sputtering was performed at a power of 85 W. Unless otherwise specified, the deposition thickness of the electrodes used for experiments and characterization was controlled at ~50 nm (Ni_{50}/ATO) by a quartz thickness gauge located in the center of the sputtering chamber. Similarly, Cu/ATO and Co/ATO electrodes were prepared by replacing the high-purity targets. More details are described in Supplementary Table 15.

Characterizations

The crystalline structure of the electrodes was characterized by X-ray diffraction (XRD, Rigaku Smartlab, Japan). The chemical structures of the electrodes were investigated using X-ray photoelectron spectroscopy (XPS, AXIS SUPRA+, Japan) and Raman spectroscopy (Renishaw inVia, England). The surface morphology and microstructures of the electrodes were obtained by field emission scanning electron microscopy (FESEM, Hitachi SU8010, Japan) and high-resolution transmission electron microscopy (HRTEM, FEI Tecnai G2 F30, America). The atomic structure and elemental composition of the catalytic layer were analyzed by aberration-corrected high-angle annular dark-field scanning TEM (AC HAADF-STEM, Thermo-Spectra 200, America) equipped with energy dispersive X-ray spectroscopy (EDS). The optical properties of the electrodes were tested by a fluorescence spectrometer (Horiba FluoroMax-4, France) and a UV-visible spectrophotometer (Shimadzu UV2450, Japan). The X-ray absorption spectroscopy (XAS), including X-ray absorption near-edge structure (XANES) and extended X-ray absorption fine structure (EXAFS) of the samples, was collected at the Beamline of TLS07A1 (Ni K-edge) and Beamline of TPS44A1 (Sn K-edge) in Taiwan National Synchrotron Radiation Research Center (NSRRC), and the relevant data analysis details are described in Supplementary Methods.

All electrochemical measurements including linear sweep voltammetry (LSV), cyclic voltammetry (CV), and electrochemical impedance spectroscopy (EIS) were performed using a three-electrode setup on an electrochemical workstation (CHI660E, China). In situ electrochemical Raman measurements were performed in a specially designed reactor consisting of a working electrode, a counter electrode (Pt wire), and a reference electrode (Ag/AgCl) (Horiba LabRAM HR, France) (Supplementary Fig. 86). All measured potentials were converted to the reversible hydrogen electrode (RHE) scale and corrected for the iR-drop as determined by EIS.

Electrocatalytic performance and analytical methods

Unless otherwise specified, the electrocatalytic performance tests were carried out in a 100 mL single-chamber reactor at a constant current density (10 mA/cm^2), and the synthesized electrode (2×2 cm^2) and Ti foil of the same area were used as anode and cathode, respectively. A 10 mg/L SMX solution containing 0.05 M Na_2SO_4 was used as the target pollutant. The factors affecting the performance were evaluated by adjusting pH, current density, electrolyte, water matrix, and pollutant type. The degradation experiments of real antibiotic wastewater were performed to evaluate the application potential of the electrode. Before the performance test, the anodes prepared by sputtering were pre-electrolyzed for 4 min to remove the metal components weakly bound to the ATO.

The concentration of organic compounds was measured by high-performance liquid chromatography (HPLC, Agilent 1260, America) equipped with a C18 column (Supplementary Table 16). The degradation degree of organic pollutants was evaluated by a total organic carbon analyzer (TOC, Shimadzu TOC-L, Japan) and a 3D excitation-emission matrix fluorescence spectrometer (Cary Eclipse, America). Active species were identified by electron spin resonance (ESR, Bruker ESR5000, Germany). The composition and leakage of metals in the electrodes were analyzed by inductively coupled plasma-optical emission spectroscopy (ICP-OES, Thermo-iCAP PRO, America). Ion concentration was measured by ion chromatography (ECO IC, Switzerland). The degradation intermediates were identified by HPLC tandem mass spectrometry (Thermo-LTQ Orbitrap XL, America). The toxicity evolution of degradation was predicted using the toxicity assessment software tool (TEST). The concentration prediction of active species was carried out by Kintecus 6.80 chemical kinetics modeling software (Supplementary Table 17). Life-cycle inventory and emission factors in the wastewater treatment using our method and the conventional routes of advanced-oxidation processes were calculated using the Ecoinvent database in SimaPro[56].

Computational methodology

The Vienna Ab Initio Package (VASP) was employed to perform all the density functional theory (DFT) calculations within the generalized gradient approximation (GGA) using the Perdew–Burke–Enzerhof (PBE) formulation[57,58]. The projected augmented wave (PAW) potentials were applied to describe the ionic cores and take valence electrons into account using a plane wave basis set with a kinetic energy cutoff of 500 eV[59,60]. Partial occupancies of the Kohn–Sham orbitals were allowed using the Gaussian smearing method with a width of 0.1 eV. The electronic energy was considered self-consistent when the energy change was smaller than 10^{-5} eV. A geometry optimization was considered convergent when the force change was smaller than 0.05 eV/Å. Grimme's DFT-D3 methodology was used to describe the dispersion interactions[61]. The vacuum spacing perpendicular to the plane of the structure was 20 Å. The Brillouin zone integral utilized the surface structures of $2 \times 2 \times 1$ Monkhorst–Pack K-point sampling.

Data availability

The data supporting the findings of the study are included in the main text and supplementary information files. Additional data are available from the corresponding author upon request. Source data are provided with this paper.

References

1. Wang, M. et al. A triple increase in global river basins with water scarcity due to future pollution. *Nat. Commun.* **15**, 880 (2024).
2. Wilkinson, J. L. et al. Pharmaceutical pollution of the world's rivers. *Proc. Natl Acad. Sci. USA* **119**, e2113947119 (2022).

3. Morin-Crini, N. et al. Worldwide cases of water pollution by emerging contaminants: a review. *Environ. Chem. Lett.* **20**, 2311–2338 (2022).
4. Gokhale, D., Hamelberg, A. F. & Doyle, P. S. Multifunctional zwitterionic hydrogels for the rapid elimination of organic and inorganic micropollutants from water. *Nat. Water* **2**, 62–71 (2024).
5. Xie, J., Zhang, C. & Waite, T. D. Hydroxyl radicals in anodic oxidation systems: generation, identification and quantification. *Water Res.* **217**, 118425 (2022).
6. Lin, H. et al. Defect engineering on a Ti_4O_7 electrode by Ce^{3+} doping for the efficient electrooxidation of perfluorooctanesulfonate. *Environ. Sci. Technol.* **55**, 2597–2607 (2021).
7. Alkhadra, M. A. et al. Electrochemical methods for water purification, ion separations, and energy conversion. *Chem. Rev.* **122**, 13547–13635 (2022).
8. Yang, C. et al. Electro-driven cycling Fenton catalysis through two-dimensional electroresponsive metal–organic frameworks for water purification. *Nat. Water* **2**, 793–802 (2024).
9. Zuo, K. et al. Electrified water treatment: fundamentals and roles of electrode materials. *Nat. Rev. Mater.* **8**, 472–490 (2023).
10. Hu, X. et al. Engineering nonprecious metal oxides electrocatalysts for two-electron water oxidation to H_2O_2. *Adv. Energy Mater.* **12**, 2201466 (2022).
11. Lu, S. & Zhang, G. Recent advances on inactivation of waterborne pathogenic microorganisms by (photo) electrochemical oxidation processes: design and application strategies. *J. Hazard. Mater.* **431**, 128619 (2022).
12. Wang, Y.-H. et al. In situ electrochemical Raman spectroscopy and ab initio molecular dynamics study of interfacial water on a single-crystal surface. *Nat. Protoc.* **18**, 883–901 (2023).
13. Martinez-Huitle, C. A., Rodrigo, M. A., Sires, I. & Scialdone, O. Single and coupled electrochemical processes and reactors for the abatement of organic water pollutants: a critical review. *Chem. Rev.* **115**, 13362–13407 (2015).
14. Zhang, J. et al. Strong metal-support interaction boosts activity, selectivity, and stability in electrosynthesis of H_2O_2. *J. Am. Chem. Soc.* **144**, 2255–2263 (2022).
15. Liu, J. et al. Interfacial component coupling effects towards precise heterostructure design for efficient electrocatalytic water splitting. *Nano Energy* **103**, 107753 (2022).
16. Xie, L. et al. The strong metal-support interactions induced electrocatalytic three- electron oxygen reduction to hydroxyl radicals for water treatment. *Proc. Natl Acad. Sci. USA* **120**, e2307989120 (2023).
17. Du, X. et al. Size-dependent strong metal-support interaction in TiO_2 supported Au nanocatalysts. *Nat. Commun.* **11**, 5811 (2020).
18. Luo, Z., Zhao, G., Pan, H. & Sun, W. Strong metal-support interaction in heterogeneous catalysts. *Adv. Energy Mater.* **12**, 2201395 (2022).
19. Shan, J. et al. Metal-metal interactions in correlated single-atom catalysts. *Sci. Adv.* **8**, 1–14 (2022).
20. Shi, Z. et al. Phase-dependent growth of Pt on MoS_2 for highly efficient H_2 evolution. *Nature* **621**, 300–305 (2023).
21. Yang, J., Li, W., Wang, D. & Li, Y. Electronic metal-support interaction of single-atom catalysts and applications in electrocatalysis. *Adv. Mater.* **32**, 2003300 (2020).
22. Zhan, P. et al. Efficient electrosynthesis of urea over single-atom alloy with electronic metal support interaction. *Angew. Chem. Int. Ed.* **63**, e202409019 (2024).
23. Gloag, L., Somerville, S. V., Gooding, J. J. & Tilley, R. D. Co-catalytic metal-support interactions in single-atom electrocatalysts. *Nat. Rev. Mater.* **9**, 173–189 (2024).
24. Li, C. et al. Self-accommodation induced electronic metal-support interaction on ruthenium site for alkaline hydrogen evolution reaction. *Adv. Mater.* **35**, 2301369 (2023).
25. Liu, Y. et al. Electronic metal-support interactions boost *OOH intermediate generation in Cu/In_2Se_3 for electrochemical H_2O_2 production. *Angew. Chem. Int. Ed.* **63**, e202319470 (2024).
26. Yang, Y. et al. Which micropollutants in water environments deserve more attention globally? *Environ. Sci. Technol.* **56**, 13–29 (2022).
27. Martinez-Huitle, C. A. & Ferro, S. Electrochemical oxidation of organic pollutants for the wastewater treatment: direct and indirect processes. *Chem. Soc. Rev.* **35**, 1324–1340 (2006).
28. Yuan, Q. et al. Degradation of antibiotics by electrochemical advanced oxidation processes (EAOPs): performance, mechanisms, and perspectives. *Sci. Total. Environ.* **856**, 159092 (2023).
29. Wang, J. et al. Engineering the coordination environment of Ir single atoms with surface titanium oxide amorphization for superior chlorine evolution reaction. *J. Am. Chem. Soc.* **146**, 11152–11163 (2024).
30. Shi, X., Back, S., Gill, T. M., Siahrostami, S. & Zheng, X. Electrochemical synthesis of H_2O_2 by two-electron water oxidation reaction. *Chem.* **7**, 38–63 (2021).
31. Popov, I. et al. Chemical kinetics of metal single atom and nanocluster formation on surfaces: An example of Pt on hexagonal boron nitride. *Nano Lett.* **23**, 8006–8012 (2023).
32. Tyndall, D. et al. Demonstrating the source of inherent instability in NiFe LDH-based OER electrocatalysts. *J. Mater. Chem. A* **11**, 4067–4077 (2023).
33. Pu, T., Zhang, W. & Zhu, M. Engineering heterogeneous catalysis with strong metal-support interactions: Characterization, theory and manipulation. *Angew. Chem. Int. Ed.* **62**, e202212278 (2023).
34. Jimenez-Morales, I., Haidar, F., Cavaliere, S., Jones, D. & Roziere, J. Strong interaction between platinum nanoparticles and tantalum-doped tin oxide nanofibers and its activation and stabilization effects for oxygen reduction reaction. *ACS Catal.* **10**, 10399–10411 (2020).
35. Yu, J. et al. Ultra-high thermal stability of sputtering reconstructed Cu-based catalysts. *Nat. Commun.* **12**, 7209 (2021).
36. Tan, W. et al. Fine-tuned local coordination environment of Pt single atoms on ceria controls catalytic reactivity. *Nat. Commun.* **13**, 7070 (2022).
37. Mameda, N. et al. Highly robust and efficient Ti-based Sb-SnO_2 anode with a mixed carbon and nitrogen interlayer for electrochemical 1,4-dioxane removal from water. *Chem. Eng. J.* **393**, 124794 (2020).
38. Ma, D. et al. Enhanced catalytic ozonation for eliminating CH_3SH via stable and circular electronic metal-support interactions of Si-O-Mn bonds with low Mn loading. *Environ. Sci. Technol.* **56**, 3678–3688 (2022).
39. Wang, H., Gao, L., Xie, Y., Yu, G. & Wang, Y. Clarification of the role of singlet oxygen for pollutant abatement during persulfate-based advanced oxidation processes: Co_3O_4@CNTs activated peroxymonosulfate as an example. *Water Res.* **244**, 120480 (2023).
40. Rao, Z. et al. Light-reinforced key intermediate for anticoking to boost highly durable methane dry reforming over single atom Ni active sites on CeO_2. *J. Am. Chem. Soc.* **145**, 24625–24635 (2023).
41. Wang, P. et al. In situ formation of cocatalytic sites boosts single-atom catalysts for nitrogen oxide reduction. *Proc. Natl Acad. Sci. USA* **120**, e2216584120 (2023).
42. Hou, M. et al. Microenvironment reconstitution of highly active Ni single atoms on oxygen-incorporated Mo_2C for water splitting. *Nat. Commun.* **15**, 1342 (2024).
43. Zhu, H. et al. High-entropy alloy stabilized active Ir for highly efficient acidic oxygen evolution. *Chem. Eng. J.* **431**, 133251 (2022).

44. Zhang, X. et al. Fast modulation of *d*-band holes quantity in the early reaction stages for boosting acidic oxygen evolution. *Angew. Chem. Int. Ed.* **62**, e202308082 (2023).
45. Wang, Y.-H. et al. In situ Raman spectroscopy reveals the structure and dissociation of interfacial water. *Nature* **600**, 81–85 (2021).
46. Wu, L. et al. Boosting hydrogen oxidation kinetics by promoting interfacial water adsorption on d-p hybridized Ru catalysts. *ACS Catal.* **13**, 4127–4133 (2023).
47. Wang, Y.-H. et al. Characterizing surface-confined interfacial water at graphene surface by in situ Raman spectroscopy. *Joule* **7**, 1652–1662 (2023).
48. Li, C.-Y. et al. In situ probing electrified interfacial water structures at atomically flat surfaces. *Nat. Mater.* **18**, 697–701 (2019).
49. Noguchi, H., Okada, T. & Uosaki, K. Molecular structure at electrode/electrolyte solution interfaces related to electrocatalysis. *Faraday Discuss.* **140**, 125–137 (2008).
50. Yang, J. et al. The electronic metal-support interaction directing the design of single atomic site catalysts: achieving high efficiency towards hydrogen evolution. *Angew. Chem. Int. Ed.* **60**, 19085–19091 (2021).
51. Yang, P. et al. Microwave quasi-solid state to construct strong metal-support interactions with interfacial electron-enriched Ru for anion exchange membrane electrolysis. *Adv. Energy Mater.* **14**, 2303384 (2024).
52. Wan, W. et al. Mechanistic insight into the active centers of single/dual-atom Ni/Fe-based oxygen electrocatalysts. *Nat. Commun.* **12**, 5589 (2021).
53. Cai, M. et al. Formation and stabilization of NiOOH by introducing α-FeOOH in LDH: composite electrocatalyst for oxygen evolution and urea oxidation reactions. *Adv. Mater.* **35**, 2209338 (2023).
54. Kurban, M. et al. Chlorine oxide radical: an emerging free radical for denitrification and pollutant degradation. *J. Environ. Chem. Eng.* **12**, 112630 (2024).
55. Zhang, G. et al. Redox-neutral electrochemical decontamination of hypersaline wastewater with high technology readiness level. *Nat. Nanotechnol.* **19**, 1130–1140 (2024).
56. Wernet, G. et al. The ecoinvent database version 3 (part I): overview and methodology. *Int. J. Life Cycle Assess.* **21**, 1218–1230 (2016).
57. Perdew, J. P., Burke, K. & Ernzerhof, M. Generalized gradient approximation made simple. *Phys. Rev. Lett.* **77**, 3865–3868 (1996).
58. Kresse, G. & Joubert, D. From ultrasoft pseudopotentials to the projector augmented-wave method. *Phys. Rev. B* **59**, 1758–1775 (1999).
59. Blochl, P. E. Projector augmented-wave method. *Phys. Rev. B* **50**, 17953–17979 (1994).
60. Grimme, S., Antony, J., Ehrlich, S. & Krieg, H. A consistent and accurate ab initio parametrization of density functional dispersion correction (DFT-D) for the 94 elements H-Pu. *J. Chem. Phys.* **132**, 154104 (2010).
61. Henkelman, G., Uberuaga, B. P. & Jónsson, H. A climbing image nudged elastic band method for finding saddle points and minimum energy paths. *J. Chem. Phys.* **113**, 9901–9904 (2000).

Acknowledgements

This work was supported by the National Natural Science Foundation of China (51978197), Guangdong Basic and Applied Basic Research Foundation (2021B1515120077), Shenzhen Science and Technology Innovation Commission (GXWD20231129091129002 and RCYX20210609103122038), and the Fundamental Research Funds for the Central Universities.

Author contributions

S.L. and G.Z. designed the research; S.L. synthesized the materials and performed experiments; S.L., X.L., and G.Z. analyzed the data; S.L., G.Z., and S.W. wrote the manuscript. All the authors discussed the results and commented on the manuscript.

Competing interests

The authors declare no competing interest.

Additional information

Supplementary information The online version contains supplementary material available at https://doi.org/10.1038/s41467-025-59722-1.

Correspondence and requests for materials should be addressed to Guan Zhang.

Peer review information *Nature Communications* thanks the anonymous reviewers for their contribution to the peer review of this work. A peer review file is available.

Sen Lu[1,2], **Xuechuan Li**[1], **Guan Zhang**[1] ✉ & **Shaobin Wang**[2]

[1]State Key Laboratory of Urban Water Resource and Environment, School of Ecology and Environment, Harbin Institute of Technology, Shenzhen (HITSZ), Shenzhen 518055, China. [2]School of Chemical Engineering, The University of Adelaide, Adelaide, SA 5005, Australia. ✉e-mail: zhangguan@hit.edu.cn